Quantum simulations of molecular systems with intrinsic atomic orbitals

Stefano Barison◉ and Davide E. Galli◉

Dipartimento di Fisica "Aldo Pontremoli", Università degli Studi di Milano, via Celoria 16, I-20133 Milano, Italy

Mario Motta◉

IBM Quantum, IBM Research Almaden, 650 Harry Road, San Jose, California 95120, USA

Quantum simulations of molecular systems on quantum computers often employ minimal basis sets of Gaussian orbitals. In comparison with more realistic basis sets, quantum simulations employing minimal basis sets require fewer qubits and quantum gates but yield results of lower accuracy. A natural strategy to achieve more accurate results is to increase the basis set size, which, in turn, requires increasing the number of qubits and quantum gates. Here we explore the use of intrinsic atomic orbitals in quantum simulations of molecules to improve the accuracy of energies and properties at the same computational cost required by a minimal basis. We investigate ground-state energies and one- and two-body density operators in the framework of the variational quantum eigensolver employing and comparing different Ansätze. We also demonstrate the use of this approach in the calculation of ground- and excited-state energies of small molecules by a combination of quantum algorithms using IBM quantum computers.

I. INTRODUCTION

The simulation of quantum many-body systems has long been recognized as an application for quantum computers [1–7]. Whereas contemporary quantum devices and algorithms have enabled the simulation of ground- and excited-state properties of a variety of systems [8], quantum computing is still an emerging technology with limited simulation capabilities. In the field of quantum chemistry, the limitations of quantum devices, classical simulators, and quantum algorithms have resulted in most quantum electronic structure simulations reported to date employing minimal basis sets of Gaussian orbitals [8–10] or active spaces constructed on the basis of preliminary correlated classical simulations [11].

Such simulations have profound theoretical interest and represent a driving force in the development of quantum devices, simulators, and algorithms, but they are far from returning the high-accuracy results needed by the quantum simulation of molecules.

Achieving this goal typically requires increasing significantly the number of qubits and quantum gates and implementing sophisticated techniques to increase the representation accuracy of qubits [12,13]. Techniques that can improve the accuracy of quantum simulations without extra quantum resources and without reliance on preliminary classical simulations, thus, become desirable.

In the present paper, we explore the use of intrinsic atomic orbitals [14,15] (IAOs) in the quantum simulation of molecular systems. IAOs define atomic core and valence orbitals, polarized by the molecular environment, which can exactly represent self-consistent field wave functions, through a remarkably simple algebraic construction [14] free from input

from correlated many-body calculations. IAOs yielded accurate evaluations of a variety of chemical properties in different environments and supported the understanding of molecular properties and the development of computational techniques [14,16–20].

Using the bond cleavage of several small molecules as an application, we demonstrate the integration of IAOs in a variety of quantum algorithms, using classical simulators of quantum computers and IBM quantum hardware. We discuss strengths and weaknesses of the migration from minimal bases to IAOs, and identify the perturbative treatment of dynamical correlation from nonvalence virtual orbitals as a way to further improve quantum simulations based on IAOs.

II. METHODS

A. Intrinsic atomic orbitals

The IAO construction aims at combining the best properties of a set of molecular orbitals (MOs) $|\chi_m\rangle = \sum_a C_{am}|\varphi_a\rangle$ computed at mean-field level in a large basis set $B_1 = \{\varphi_a\}_a$, and of a valence basis $B_2 = \{\tilde{\rho}_b\}_b$ of atomic orbitals (AOs). Here, given a molecule with geometry $G = \{(Z_k, \mathbf{R}_k)\}_{k=1}^{N_A}$, where Z_k's are the atomic numbers and $\mathbf{R}_k$'s are the positions of the constituent atoms, we choose $B_1 = \bigcup_k B(Z_k; \mathbf{R}_k)$, where $B(Z_k; \mathbf{R}_k)$ is a set of Gaussian orbitals for atom k (e.g., Dunning's correlation consistent bases with polarized and multiple valence orbitals, usually abbreviated in cc-pVxZ [21]). On the other hand, to construct B_2, for every atom in the molecule we perform a single-atom Hartree-Fock calculation with basis $B(Z_k; \mathbf{R}_k)$, yielding a set of core, valence, and external orbitals for that particular atom, and we append the core and valence orbitals to the basis B_2. Since a common

022404-1

set of single-atom bases $B(Z_k; \mathbf{R}_k)$ is used in the construction of both B_1 and B_2, then B_2 is a proper subset of B_1.

The MOs can, of course, reproduce the mean-field wave function from which they are defined but cannot be clearly associated with any atom, which complicates the interpretation of the wave function and of its properties. The AOs, although naturally associated with an atom, give an inaccurate representation of the MOs as they contain no polarization due to the molecular environment. The IAO basis is then constructed by forming a set of polarized AOs $\{\rho_b\}_b$ that at variance with the AOs in B_2 can exactly express occupied MOs $|\chi_i\rangle$. First, the projectors $P = \sum_i |\chi_i\rangle\langle\chi_i|$, $Q = \mathbb{1} - P$ onto occupied and virtual MOs are defined. This allows to define the projectors,

$$
\begin{aligned}
P_{12} &= \sum_{\phi_a, \phi_b \in B_1} S^{ab} |\phi_a\rangle\langle\phi_b|, \\
P_{21} &= \sum_{\tilde{\rho}_c, \tilde{\rho}_d \in B_2} \tilde{S}^{cd} |\tilde{\rho}_c\rangle\langle\tilde{\rho}_d|,
\end{aligned}
\tag{1}
$$

onto the bases B_1 and B_2, where S^{ab} and $\tilde{S}^{cd}$ are the inverse overlap matrices in B_1 and B_2, respectively. Then, a set of depolarized occupied MOs $|\tilde{\chi}_i\rangle = P_{12}P_{21}|\chi_i\rangle$ is constructed by projecting the original, polarized, occupied MOs onto the AO basis B_2, and immersing the projected MOs in the original basis B_1. The depolarized occupied MOs are used to define the projectors $\tilde{P} = \sum_i |\tilde{\chi}_i\rangle\langle\tilde{\chi}_i|$ and $\tilde{Q} = \mathbb{1} - \tilde{P}$, and the IAOs are obtained as

$$
|\rho_b\rangle = (P\tilde{P} + Q\tilde{Q})P_{12}|\tilde{\rho}_b\rangle. \tag{2}
$$

Therefore, IAOs are constructed through a sequence of simple and natural algebraic operations. In addition to the projection (2), we orthonormalize the IAO basis to ensure the satisfaction of canonical anticommutation relations between second-quantization operators, and we perform a Foster-Boys localization of the IAOs to enhance their spatial locality [22].

Finally, we consider the Born-Oppenheimer approximation of the molecular Hamiltonian [23],

$$
H = E_0 + \sum_{\substack{pq \\ \sigma}} h_{pq} \hat{c}_{p\sigma}^\dagger \hat{c}_{q\sigma} + \sum_{\substack{prqs \\ \sigma\tau}} \frac{(pr|qs)}{2} \hat{c}_{p\sigma}^\dagger \hat{c}_{q\tau}^\dagger \hat{c}_{s\tau} \hat{c}_{r\sigma}, \tag{3}
$$

where E_0 indicates the repulsion between nuclei of the molecule, h_{pq} is the one-body part of the Hamiltonian, containing kinetic energy of the electron plus the interaction with the fixed nuclei, and $(pr|qs)$ is the electron-electron repulsion integral. Once the IAOs are defined, we fold the Hamiltonian in Eq. (3) through a standard atomic orbitals to molecular orbitals (ao2mo) transformation from the B_1 to the orthonormalized IAO basis. In this paper, we relied on the frozen-core approximation since the basis sets we employed lack core-valence correlation effects.

B. Ground- and excited-state algorithms

We explored the ground and excited states of the Hamiltonian (3) with several techniques. Here, we focused on the the variational quantum eigensolver [24,25] and quantum imaginary-time evolution [26] methods for ground-state studies. In Appendix B, we also investigate the quantum equation-of-motion [27] method for excited-state studies.

1. Variational quantum eigensolver

Variational quantum state preparation algorithms are widely used on contemporary quantum devices. These algorithms define a set of Ansatz states approximating the ground state of a target Hamiltonian, of the form $|\Psi(\theta)\rangle = \hat{U}(\theta)|\Psi_0\rangle$, $\theta \in \Theta \subseteq \mathbb{R}^n$. In other words, a parametrized quantum circuit $\hat{U}(\theta)$ is applied to an initial wave-function $|\Psi_0\rangle$. The best approximation to the ground state in the set of Ansatz states is found by minimizing the energy $E(\theta) = \langle\Psi(\theta)|\hat{H}|\Psi(\theta)\rangle$ as a function of the parameters θ using a classical optimization algorithm [24,25]. This algorithmic work flow, termed variational quantum eigensolver (VQE) [24] in the quantum simulation literature, is a heuristic technique for ground-state approximation. Its accuracy and computational cost are determined by the form of the circuit $\hat{U}(\theta)$'s.

Within VQE, we compare different Ansätze $\hat{U}(\theta)$:

(1) The quantum unitary coupled cluster with single and double excitations (q-UCCSD), where $\hat{U}(\theta)$ is a qubit representation of the operator [28–31],

$$
\begin{aligned}
\hat{U}_{\text{q-UCCSD}}(\theta) &= e^{\hat{T} - \hat{T}^\dagger}, \\
\hat{T} &= \sum_{ai} \theta_i^a \hat{c}_a^\dagger \hat{c}_i + \sum_{abij} \theta_{ij}^{ab} \hat{c}_a^\dagger \hat{c}_b^\dagger \hat{c}_j \hat{c}_i,
\end{aligned}
\tag{4}
$$

with ij occupied and ab virtual in the mean-field reference state. The q-UCCSD quantum circuit is given in Ref. [31].

(2) The hardware-efficient R_y Ansatz with linear connectivity [8] which, for a register of n qubits and an Ansatz of depth d, takes the form

$$
\hat{U}_{R_y}(\theta) = \left[\prod_{i=0}^{n-1} \hat{R}_y^{(i)}(\theta_i^d)\right] \prod_{\ell=0}^{d-1}\left[\prod_{i=0}^{n-2} U_{i,i+1}^{\text{ent}} \prod_{i=0}^{n-1} \hat{R}_y^{(i)}(\theta_i^\ell)\right], \tag{5}
$$

where $U_{i,i+1}^{\text{ent}}$ is an entangler gate of choice, in this case a controlled-NOT (CNOT) gate with control qubit i and target qubit $i + 1$, and $\hat{R}_y^{(i)}(\theta_i^\ell)$ is the ℓth Y rotation of qubit i by an angle θ_i^ℓ,

(3) the hardware-efficient SO(4) Ansatz, of the form

$$
\hat{U}_{\text{SO}(4)}(\theta) = \prod_{\ell=0}^{d-1}\left[\prod_{(ij)\in N} \hat{u}_{ij}(\theta_{ij}^\ell)\right], \tag{6}
$$

where u_{ij} is a two-qubit gate in the SO(4) group. It is well known [32] that a two-qubit gate in the SO(4) group can be written (as shown in Fig. 3) as a product of two Hadamard, four S, two CNOT, and two single-qubit u_3 gates. Single-qubit u_3 gates are defined as

$$
u_3(\theta, \phi, \lambda) = R_z(\phi) R_x\left(-\frac{\pi}{2}\right) R_z(\theta) R_x\left(\frac{\pi}{2}\right) R_z(\lambda), \tag{7}
$$

where θ, ϕ, and λ are three angles and $R_{x,y,z}$ are single-qubit X, Y, and Z rotations, respectively.

2. Quantum imaginary-time evolution

Quantum imaginary-time evolution (QITE) [26,33–36] is an alternative and complementary technique to VQE and other heuristic quantum algorithms for a ground-state search. QITE is an Ansatz-independent technique that approaches the ground state of a quantum system by applying the following

imaginary-time evolution (ITE) map on a trial wave-function $|\Psi_T\rangle$,

$$|\Psi_\beta\rangle = \frac{e^{-\beta\hat{H}}|\Psi_T\rangle}{|e^{-\beta\hat{H}}\Psi_T|}. \tag{8}$$

The ITE is divided in a large number n_β of steps of length $\Delta\tau = \beta/n_\beta$ and ITE under a single step is approximated by a Trotter decomposition,

$$e^{-\beta\hat{H}} \simeq \prod_m e^{-\beta\hat{h}[m]}, \tag{9}$$

where $\hat{H} = \sum_m \hat{h}[m]$ is a representation of the Hamiltonian as a sum of local operators. ITE under a single imaginary-time step and a single local term of the Hamiltonian is approximated by a unitary transformation, that is, equal to the exponential of a linear combinations of local operators P_μ,

$$\frac{e^{-\Delta\tau\hat{h}[\mu]}|\Psi\rangle}{|e^{-\Delta\tau\hat{h}[\mu]}\Psi|} \simeq \exp\left(i\sum_\mu x_\mu P_\mu\right)|\Psi\rangle. \tag{10}$$

The coefficients x_μ are determined [26] solving a linear system of the form $Ax = b$ with

$$A_{\mu\nu} = \langle\Psi|P_\mu P_\nu|\Psi\rangle, \qquad b_\mu = \langle\Psi|P_\mu\hat{h}[m]|\Psi\rangle. \tag{11}$$

The QITE simulations reported in this paper are carried out in a two-orbital space. For such a problem, additional simplifications are possible, which are listed and discussed in Appendix D.

C. Evaluation of density matrices

Once the optimal state $|\Psi\rangle$ is found, ground-state properties can be computed as expectation values of suitable qubit operators. Here we consider the case of one- and two-body density matrices,

$$\begin{aligned} \rho_{pr}^{(\sigma)} &= \langle\Psi|\hat{c}_{p\sigma}^\dagger\hat{c}_{r\sigma}|\Psi\rangle, \\ \rho_{prqs}^{(\sigma,\tau)} &= \langle\Psi|\hat{c}_{p\sigma}^\dagger\hat{c}_{q\tau}^\dagger\hat{c}_{s\tau}\hat{c}_{r\sigma}|\Psi\rangle, \end{aligned} \tag{12}$$

which are useful for a variety of applications from computing correlation functions to understanding electron entanglement, molecular bonding [37–39], and performing orbital relaxation [40–42].

The operators (12) can be mapped onto qubit operators using standard techniques. For example, in the Jordan-Wigner [43–45] representation,

$$\hat{c}_{p\sigma}^\dagger = \begin{cases} (S_+)_p \sigma_{p-1}^z \cdots \sigma_0^z, & \sigma =\uparrow, \\ (S_+)_{n+p} \sigma_{n+p-1}^z \cdots \sigma_0^z & \sigma =\downarrow, \end{cases} \tag{13}$$

where

$$S_+ = \frac{\sigma^x + i\sigma^y}{2} \quad \text{and} \quad S_- = \frac{\sigma^x - i\sigma^y}{2}, \tag{14}$$

n is the size of the IAO basis and σ^μ with $\mu \in \{x, y, z\}$ are the standard Pauli x, y, and z operators, respectively. Therefore,

$$\rho^{(\sigma)} = \langle\Psi|X_{pr}^\sigma|\Psi\rangle, \tag{15}$$

with

$$X_{pr}^\uparrow = \begin{cases} (S_+)_p \sigma_{p-1}^z \cdots \sigma_{r+1}^z (S_-)_r, & \text{if } p > r, \\ \frac{1-\sigma_p^z}{2}, & \text{if } p = r, \\ (S_-)_r \sigma_{r-1}^z \cdots \sigma_{p+1}^z (S_+)_p, & \text{if } p < r, \end{cases} \tag{16}$$

and

$$X_{pr}^\downarrow = \begin{cases} (S_+)_{p+n} \sigma_{p+n-1}^z \cdots \sigma_{r+n+1}^z (S_-)_r, & \text{if } p > r, \\ \frac{1-\sigma_{n+p}^z}{2}, & \text{if } p = r, \\ (S_-)_{r+n} \sigma_{r-1}^z \cdots \sigma_{p+n+1}^z (S_+)_{p+n}, & \text{if } p < r. \end{cases} \tag{17}$$

In a similar way,

$$\rho_{prqs}^{(\sigma\tau)} = \langle\Psi|X_{pr}^\sigma X_{qs}^\tau|\Psi\rangle - \delta_{qr}\delta_{\sigma\tau}\langle\Psi|X_{ps}^\sigma|\Psi\rangle. \tag{18}$$

D. Variational quantum subspace expansion

Incorporating dynamical correlation from nonvalence virtual orbitals is important to improve the quantitative accuracy of simulations based on IAOs: Here, we demonstrate how to partly overcome this limitation using a simplified implementation of the virtual quantum subspace expansion technique (VQSE). This technique, proposed by Takeshita *et al.* [12], introduces contributions from virtual orbitals lying outside a chosen active space in a systematic way. The starting point of VQSE is a reference function Ψ_0 constructed in a set of active orbitals from a large basis. Here, active-space orbitals are linear combinations of IAOs, denoted with lowercase letters $p \in A$. Uppercase letters $P \in B_1$ denote orthonormal orbitals in the basis used to construct IAOs.

Next, VQSE introduces a set of expansion operators. Here, we choose

$$\begin{aligned} |\Psi\rangle &= [\alpha + \beta_{Pr}\hat{c}_{P\sigma}^\dagger\hat{c}_{r\sigma} + \gamma_{TuVw}\hat{c}_{T\sigma}^\dagger\hat{c}_{V\tau}^\dagger\hat{c}_{w\tau}\hat{c}_{u\sigma}]|\Psi_0\rangle \\ &= [\alpha + \beta_{Pr}E_{Pr} + \gamma_{TuVw}E_{TuVw}]|\Psi_0\rangle. \end{aligned} \tag{19}$$

Electrons are excited from active to generic orbitals, excitation operators are summed over spin polarizations σ, τ, and Einstein's summation convention is used. Note that the reference wave function has no components outside the active space A, and, therefore, contraction over orbitals outside A can be computed analytically using Wick's theorem.

The amplitudes $v = (\alpha\ \beta\ \gamma)^T$ are real valued and determined by solving a generalized eigenvalue equation $Hv = ESv$.

Detailed calculation to obtain the explicit form of H and S can be found in Appendix E. The matrix elements of H and S are evaluated using data from a quantum device and, subsequently, diagonalized on a classical computer to extract the lowest eigenvalue. Although we relied on full diagonalization and extraction of the lowest eigenvalue for simplicity, a better scaling with basis size could easily be achieved using Davidson's algorithm.

In the present paper, we focused on two-electron problems where the the explicit forms of H and S are defined by the active-space one- and two-body density matrices [12] that we introduced in Sec. II C.

E. Software for classical and quantum simulations

The calculations performed here involved initial preprocessing using the PYSCF quantum chemistry package [46,47].

TABLE I. Dissociation energy and equilibrium bond length for different molecules using various VQE Ansätze at STO-6G and the IAO-aug-cc-pVQZ level of theory and from CCSD at the aug-cc-pVQZ level of theory. The table also reports the values obtained with the Full Configuration Interaction (FCI) method. From here on, except when explicitly stated, the energies are reported in Hartree units (E_h) and atomic distances in Angstrom units (Å).

Basis	Method	H_2		HeH^+		LiH		H_2O		NH_3	
		ΔE (E_h)	R_{eq} (Å)	ΔE (E_h)	R_{eq} (Å)	ΔE (E_h)	R_{eq} (Å)	ΔE (E_h)	R_{eq} (Å)	ΔE (E_h)	R_{eq} (Å)
	HF	N/A	0.695(9)	N/A	0.937(9)	N/A	1.482(5)	N/A	0.993(1)	N/A	1.024(2)
	$R_y, d = 1$	0.2084(9)	0.715(7)	0.0513(3)	0.919(1)	0.0833(7)	1.482(7)	0.1353(1)	0.970(7)	0.1525(7)	1.024(3)
STO-6G	SO(4), $d = 1$	0.2083(9)	0.715(7)	0.0513(3)	0.919(1)	0.0837(6)	1.482(8)	0.1358(4)	0.941(5)	0.1510(6)	1.024(2)
	q-UCCSD	0.2083(9)	0.715(7)	0.0513(3)	0.919(1)	0.1079(9)	1.522(1)	0.1625(8)	1.006(5)	0.1694(4)	1.058(2)
	FCI	0.2092(2)	0.715(7)	0.0512(7)	0.919(4)	0.1075(5)	1.522(2)	0.1626(0)	1.006(7)	0.1694(4)	1.058(2)
	HF	N/A	0.716(4)	N/A	0.770(4)	N/A	1.586(5)	N/A	0.949(7)	N/A	0.995(1)
	$R_y, d = 1$	0.1721(7)	0.729(9)	0.0822(9)	0.768(4)	0.10589	1.586(6)	0.1755(7)	0.921(9)	0.1774(9)	0.996(3)
IAO	SO(4), $d = 1$	0.1721(7)	0.729(9)	0.0822(9)	0.768(4)	0.1000(2)	1.584(2)	0.1861(8)	0.924(8)	0.1760(6)	0.996(1)
	q-UCCSD	0.1760(5)	0.729(9)	0.0822(9)	0.768(4)	0.1362(0)	1.612(9)	0.1978(2)	0.965(6)	0.1849(6)	1.022(1)
	FCI	0.1721(7)	0.729(9)	0.0822(6)	0.767(8)	0.1362(0)	1.612(9)	0.1924(2)	0.965(8)	0.1923(4)	1.023(1)
aug-cc-pVQZ	CCSD	0.1798(4)	0.719(7)	0.0752(3)	0.774(6)	0.1388(2)	1.572(9)	0.2309(1)	0.959(8)	0.2139(9)	1.007(8)

PYSCF was used to generate optimized mean-field states, Hamiltonian matrix elements in the IAO basis, and a reaction path for the $NH_3 \rightarrow NH_2 + H$ reaction by a collection of constrained geometry optimizations performed using Moller-Plesset perturbation theory [48] in a correlation-consistent Dunning's basis, augmented with an extra diffuse function in each orbital angular momentum (MP2/aug-cc-pVTZ). The restricted closed-shell Hartree-Fock (RHF) singlet state was chosen as the initial state for all of the calculations described here. Intrinsic atomic orbitals are computed as detailed in Sec. II A, and IAOs obtained from an underlying basis B are denoted as IAO/B.

Having selected a set of single-electron orbitals for each of the studied species, quantum computations were performed with quantum simulators and hardware. We used IBM's open-source library for quantum computing QISKIT [49]. In particular, the library contains implementations of techniques to map the fermionic Fock space onto the Hilbert space of a register of qubits, and implementations of VQE and the quantum equation of motion. In addition, a module for QITE simulations was composed using QISKIT subroutines. We use the tapering-off technique [50,51] to account for molecular point-group symmetries and reduce the number of qubits required for a simulation whenever possible.

In VQE simulations, we minimized the expectation value of the Hamiltonian with respect to the parameters in the circuit. On simulators, optimizations were carried out using the L-BFGS-B and CG methods [52,53], using the state-vector simulator of QISKIT. On quantum hardware, optimizations were carried out using the gradient descent optimization method described in Appendix C 1. We performed quantum computations on quantum hardware using various five-qubit IBM quantum devices, specifically *ibmq_rome*, *ibmq_vigo*, and *ibmq_london*.

F. Error mitigation techniques

In order to improve the quality of noisy hardware experiments, we referred to readout error mitigation techniques included in QISKIT [54].

In particular, we used measurement calibration to mitigate measurement errors. Given a system of N qubits, all 2^N basis input states are prepared, and the probability of measuring counts in the other basis states is computed. From these results, a calibration matrix is created and used to improve the results of subsequent experiments.

All the experiments proposed in this paper required two qubits and no more than two CNOTs, indicating that the dominant source of noise was measurement error. Running the four calibration circuits was sufficient to obtain good quality results.

Computing the calibration matrix becomes quickly unfeasible as the number of qubits increases for this reason more efficient methods have been proposed [55]. When the depth of the circuit is increased, gate errors will play a significant role on the quality of the results. In this case, gate error mitigation techniques can be adopted, such as zero noise, Richardson extrapolation [54,56–58], or probabilistic error cancellation [59].

III. RESULTS

A. Comparison between minimal bases and IAO

The migration from minimal to IAO bases in quantum and classical simulations of molecules has benefits and limitations. On the one hand, use of IAOs reduces basis set errors at mean-field level because IAOs are designed to reproduce mean-field results. Whereas basis set errors still affect chemical properties, and, particularly, correlation energies and response functions, their removal at mean-field level can improve the accuracy of many computational predictions especially in chemical species that are sensitive to the presence of polarized and diffuse functions. Furthermore, IAOs are based on a computationally inexpensive and general-purpose procedure, that enables accurate calculations of a variety of chemical properties [14,16–20], and does not resort to preliminary correlated many-body calculations, e.g., of MP2 or complete active space self-consistent field (CASSCF) type, which need to be converged and carefully designed to avoid biasing chemical properties [19,60–63].

The main limitation stemming from the use of IAOs is the presence of residual basis set errors, which can only be removed by simulating orbitals beyond the IAO basis, or with additional postprocessing. However, unlike minimal bases, IAO bases are naturally embedded into a larger basis of one-electron orbitals because they are constructed from such a basis. As a result, IAOs can be employed to capture static electronic correlation in a valence space, while dynamical correlation originating from electronic transitions to orbitals outside the IAO space can be treated perturbatively as in classical complete active space second-order perturbation theory (CASPT2) [64–66] and second-order N-electron valence state perturbation theory calculations (NVPT2) [67–69], or in recently proposed quantum-computing methods, such as VQSE [12]. In this sense, the migration from minimal to IAO bases can constitute an opportunity to integrate techniques to perturbatively capture dynamical correlation in the work flow of quantum simulations as well as to compare, demonstrate, and develop such techniques.

To illustrate the difference between minimal and IAO bases, in Table I we study the dissociation of a single H atom from a few molecules, namely, H_2, HeH^+, LiH, H_2O, and NH_3. We evaluate the ground-state energy along the dissociation path at minimal basis sets STO-6G and IAO/aug-cc-pVQZ level, using RHF and VQE with R_y, SO(4), and q-UCCSD Ansätze. As an approximation to the complete basis set limit, we perform a coupled cluster calculation with single and double excitations (CCSD) in the aug-cc-pVQZ basis (CCSD/aug-cc-pVQZ) [70]. Table I reports equilibrium bond lengths R_{eq} and binding energies ΔE.

For all studied species, FCI/IAO and q-UCCSD/IAO binding energies are in better agreement with CCSD/aug-cc-pVQZ binding energies than their counterparts at the STO-6G level. In particular, the mean absolute deviation $|\delta E(\text{FCI}/\text{-})-\delta E\text{CCSD/aug-cc-pVQZ}|$ between FCI/IAO and FCI/STO-6G binding energies is 0.015(1) Hartree, whereas for FCI/STO-6G binding energies it is 0.039(1) Hartree. The improvement is more modest for hardware-efficient Ansätze, which is not unexpected, in view of their heuristic nature. Correspondingly, the mean absolute deviation $|R_{eq}(\text{FCI/IAO})-R_{eq}(\text{CCSD/aug-cc-pVQZ})|$ between FCI/IAO and FCI/STO-6G binding energies is 0.016(1) Å, whereas for FCI/STO-6G equilibrium bond lengths it is 0.059(1) Å.

In Fig. 1, we report the complete ground-state potential-energy curve along the $NH_3 \rightarrow NH_2 + H$ reaction path. We observe that VQE/q-UCCSD provides results of FCI-like accuracy, whereas R_y and SO(4), although describing in a qualitatively correct way the dissociation limit, produce results of lower quality at lower computational cost. The deviation between hardware-efficient Ansatze and only q-UCCSD is maximal around the valley-ridge inflexion point $R \simeq 1.75$ Å, where the wave function has maximally multireference character.

B. Hardware experiments

In this subsection, we describe hardware experiments. As an illustrative application, in Fig. 2, the potential-energy surface of H_2 is computed using VQE with IAO/aug-cc-pVQZ
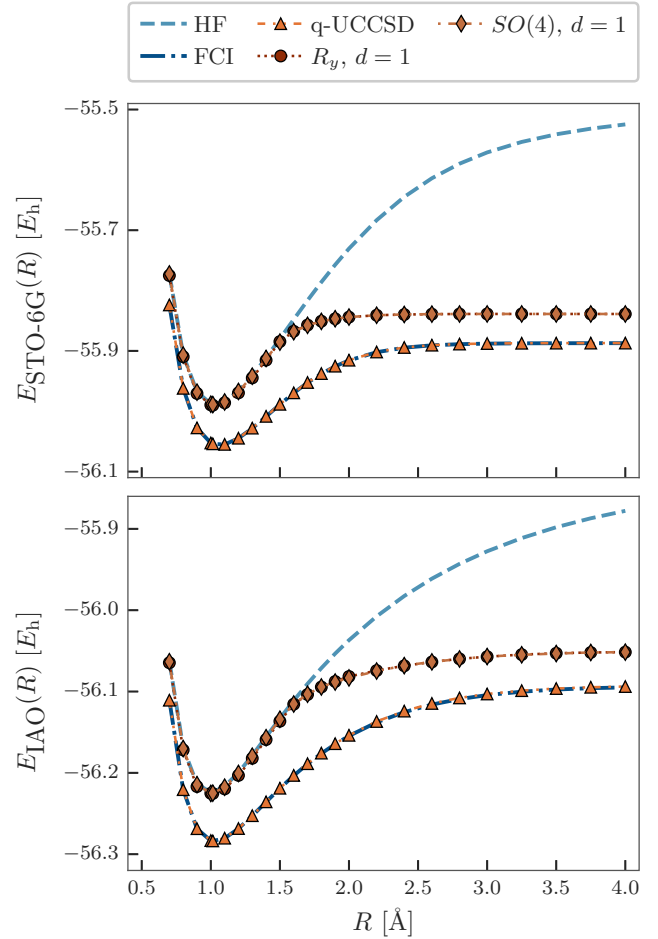

FIG. 1. Ground-state potential-energy curve of NH_3 along the $NH_3 \rightarrow NH_2 + H$ reaction path, at STO-6G (top) and IAO-aug-cc-pVQZ (bottom) level using RHF (dashed light blue line), FCI (dark blue dashed-dot line), VQE with R_y (red circles), SO(4) (dark orange diamonds), and q-UCCSD Ansätze (orange triangles). d indicates the depth of the Ansatz.

basis. Simulations required two qubits from the *ibmq_rome* device and employed an R_y Ansatz with depth $d = 1$. Given the simplicity of this application, VQE results are statistically compatible with FCI results obtained at the IAO-aug-cc-pVTZ level (agreement between orange triangles and line). As discussed in the previous section, improve the prediction of binding energies and equilibrium bond lengths over STO-6G (dotted line). The VQE on IAO/aug-cc-pVTZ results correspond to the simulation of the full valence space of H_2 but are not sufficient to recover aug-cc-pVTZ results because virtual orbitals outside the IAO basis are not included in the simulation (deviation between orange dashed-dot-dot and dark blue dashed curves). We illustrate how this limitation can be overcome by computing VQSE energies, which are statistically compatible with FCI/aug-cc-pVTZ energies (agreement between red points and line).

As a more interesting application, in the remainder of this subsection, we present the dissociation of NH_3. Studying the full seven-orbital IAO basis requires 14 qubits using a second-quantization encoding, which can be reduced to 11
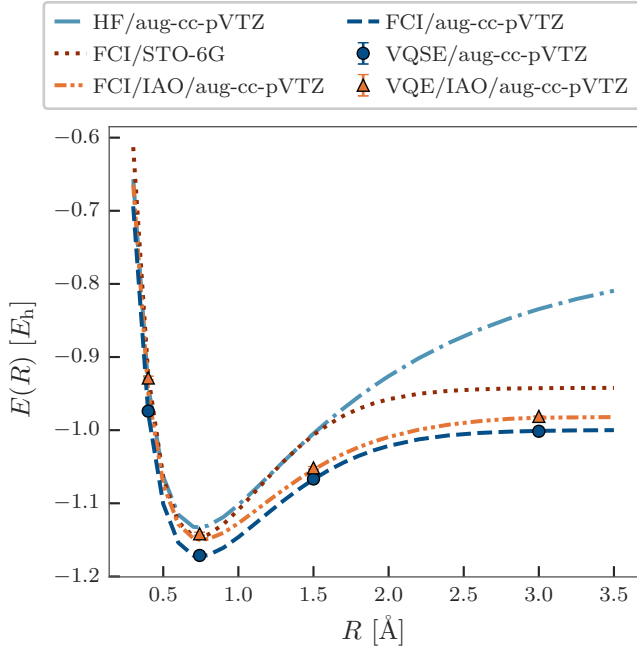
FIG. 2. Ground-state potential-energy surface of H_2 calculated using VQE and FCI with an IAO/aug-cc-pVTZ basis (orange triangles and dashed-dot-dot lines) and VQSE and FCI with full aug-cc-pVTZ basis (dark blue circles and dashed line). Statistical uncertainties on the lowest eigenvalue were obtained by sampling the active-space density matrices ten times, repeating the embedding, contraction, and diagonalization procedures for each sample, and collecting statistics with standard procedures.

or seven using qubit-reduction techniques [50,71]. For illustrative purposes and in order to use a number of qubits and gates compatible with simulation on five-qubit devices, we constructed an active space from the IAO-aug-cc-pVQZ basis.

Specifically, for every geometry along the reaction path, we performed an MP2 calculation in the IAO-aug-cc-pVQZ basis. Structures were relaxed in the estimation of the binding energies. We constructed an active space using the highest-unoccupied and the lowest-unoccupied natural orbitals (HONO-LUNO active space).

The HONO and LUNO are linear combinations of the $1s$-like IAO for H and a $2p$-like IAO for N, directed along the NH_2-H axis. Such linear combinations have σ and σ^* characters as seen in Fig. 3.

The quantum circuit used to simulate the ground state of NH_3 is shown in Fig. 3. Qubits are entangled through a SO(4) gate, parametrized leveraging the isomorphism between SO(4) and SU(2) [32,72]. Parameters are optimized using a combination of analytical gradient evaluation [73] and the gradient descent technique as illustrated in Appendix C 1. The VQE ground-state potential-energy curve is shown in Fig. 4. As seen, VQE improves significantly over RHF in the active space and yields results in qualitative agreement with FCI.

We emphasize that the use of the full-valence IAO basis as in the H_2 application is known to be reasonable from a chemical standpoint. Any other active space construction, as in the NH_3 application, needs to be supported on chemical grounds
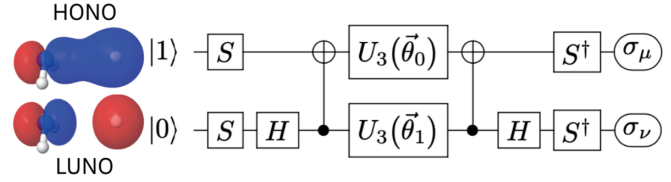

FIG. 3. Left: HONO, top and LUNO, bottom natural orbitals from an MP2 calculation using the IAO/aug-cc-pVQZ basis. Right: quantum circuit for the VQE calculations with SO(4) Ansatz in the HONO-LUNO subspace. U_3 denotes an SU(2) gate, parametrized by three Euler angles. σ^μ and σ^ν are Pauli operators appearing in the qubit representation of the active space Hamiltonian, $\hat{H} = \sum_{\mu\nu=0}^{3} \eta_{\mu\nu} \sigma^\mu \otimes \sigma^\nu$.

or assessed with numerical data. To assess the accuracy of the HONO-LUNO active space and of our VQE simulations in Table II we list active-space equilibrium bond lengths, binding energies, as well as the mean deviation,

$$\Delta_{\text{RHF,VQE}} = \sum_{i=1}^{N_R} \frac{|E_{\text{RHF,VQE}}(R_i) - E_{\text{FCI}}(R_i)|}{N_R}, \quad (20)$$

of RHF and VQE results from FCI. Results indicate that VQE accurately reproduces FCI quantities within the HONO-LUNO active space. Comparison between Tables I and II, on the other hand, indicates that the HONO-LUNO active space leads to a slightly shorter equilibrium bond length than with the full IAO basis, and to a less accurate binding energy. This is not unexpected, as the active space approximation affects the electronic structure to a varying extent along the dissociation profile.

1. Assessment of accuracy

Besides computing energies, it is important to gain as much insight as possible into the structure of the ground-state wave function. To achieve this goal, we compute the total spin operator S^2. Whereas such a quantity is a constant of motion in simulations conducted on quantum hardware it may feature significant errors due to decoherence. As seen in Fig. 5, the VQE wave function is essentially in the singlet manifold $S^2 = 0$, but is not an eigenfunction of S^2. Deviations from $S^2 = 0$ become slightly more intense for $R \geqslant 1.5$ Å, where the lowest-energy singlet and triplet states become nearly degenerate. Furthermore, we perform quantum state tomography

TABLE II. N-H dissociation energy, NH_3 equilibrium bond length, and deviation from FCI from RHF and VQE with depth-1 SO(4) Ansatz using a HONO-LUNO active space determined at IAO-aug-cc-pVQZ level.

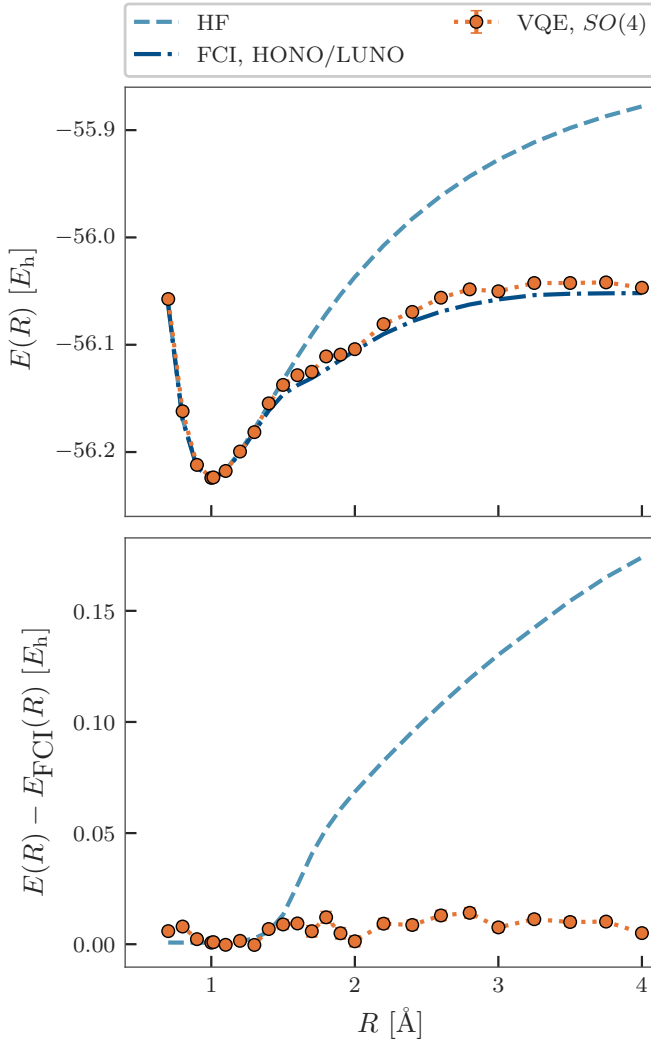| Method	ΔE (E_h)	R_{eq} (Å)	$\Delta_{\text{RHF,VQE}}$ (E_h)
RHF	N/A	0.995(1)	0.060
VQE, SO(4), $d=1$	0.165(3)	1.007(3)	0.0032(17)
FCI	0.180(2)	0.9961(7)	N/A

FIG. 4. Top: ground-state potential-energy surface of NH_3 along the $NH_3 \rightarrow NH_2 + H$ reaction path, using a HONO-LUNO active space based on an MP2 calculation at IAO/aug-cc-pVQZ level from RHF (dashed light blue line), FCI (blue dashed-dot line) and VQE with depth-1 $SO(4)$ Ansatz (orange circles). Bottom: deviation of RHF and VQE energies from FCI.

FIG. 5. Expectation values of the total spin operator (top) and purity of the VQE density operator (bottom) as a function of the reaction coordinate R, evaluated over the VQE wave function with the $SO(4)$ Ansatz. Orange and blue symbols denote hardware calculations carried out on *ibmq_rome* and on a a classical simulator with noise model from *ibmq_manila*, respectively.

(QST) [74–77] over the VQE density operator ρ_{VQE},

$$\rho_{VQE} = \sum_{\mu\nu=0}^{3} \frac{Tr[\rho_{VQE}(\sigma^\mu \otimes \sigma^\nu)]}{4}(\sigma^\mu \otimes \sigma^\nu), \qquad (21)$$

where σ^μ is a Pauli operator with $\mu \in \{id, x, y, z\}$ and σ^{id} is the identity operator. Using information from QST, we evaluate the purity $P(\rho_{VQE}) = Tr(\rho_{VQE}^2)$ of the VQE density operator. $P(\rho) = 1$ if and only if ρ is the projector $\rho = |\Psi\rangle\langle\Psi|$ onto a pure state Ψ. As seen in Fig. 5, for $R \geqslant 1.5$ Å we observe $P(\rho) \simeq 0.955$. The observed decrease in purity signals decoherent interaction with the environment, that ultimately limits the accuracy of VQE simulations.

To elucidate the origin of the deviations from $S^2 = 0$ and purity $P[\rho] = 1$, in Fig. 5 we compute these quantities on a classical simulator with noise model from *ibmq_manila*. Whereas noise models capture decoherence only partially, we
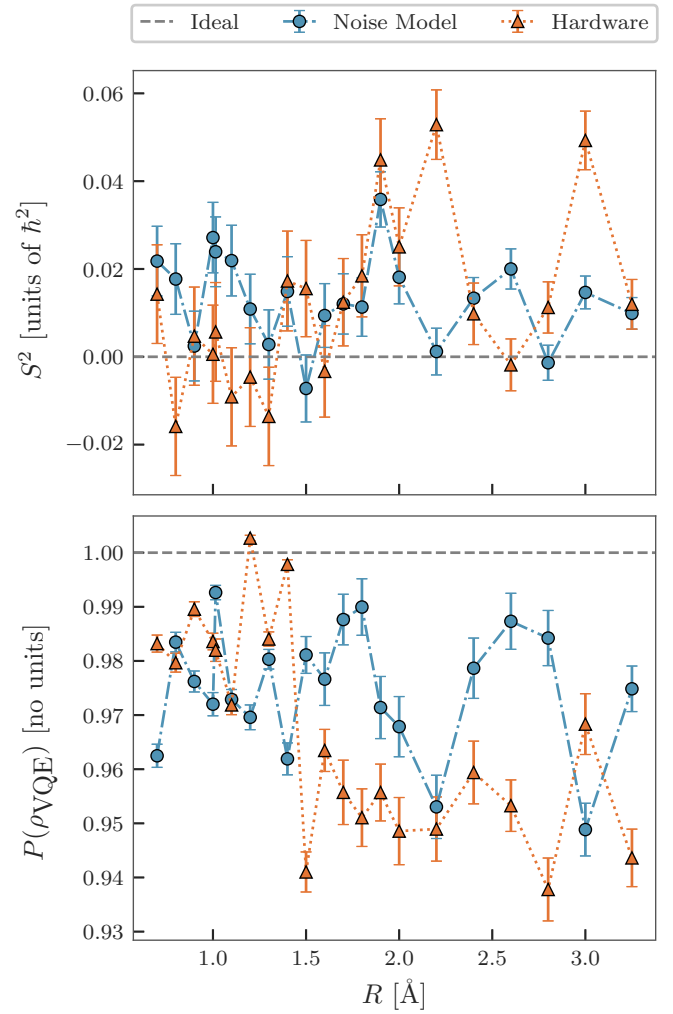
regard these data as an indication that the loss of accuracy seen here is explained by a combination of well-understood [49] qubit decoherence (amplitude damping, dephasing errors), measurement, and gate error (coherent and incoherent) mechanisms. In particular, since qubit decoherence and measurement errors affect these simulations uniformly across dissociation, the main source of error is represented by gates.

2. Density matrices

The results shown in the previous Sec. III B 1 are mostly based on QST which, despite many recent theoretical and algorithmic improvements, remains an expensive operation with growing number N_q of qubits [78–82].

An alternative way to obtain information about an electronic quantum state is provided by the one- and two-body density matrices, which can be obtained measuring up to $O(N_q^5)$ qubit operators.
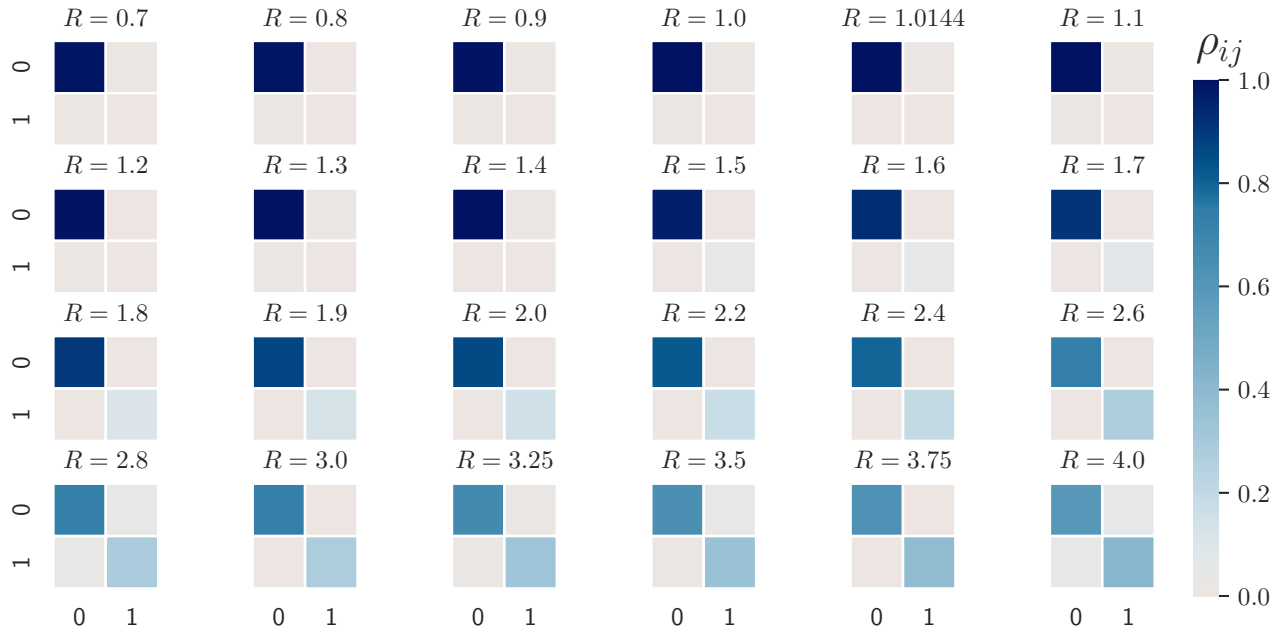
FIG. 6. Spin-resolved one-body density matrix $\rho^{(\uparrow)}$ for NH_3 in a HONO-LUNO space from VQE with the SO(4) Ansatz as a function of N-H distance (left to right, top to bottom).

One- and two-body density matrices are shown in Figs. 6 and 7, respectively. The eigenvalues of the one-body density matrix evolve from (1,0) to (1/2, 1/2) as R increases, signaling that electrons become increasingly more entangled as the H atom separates from the NH_2 moiety. The same information is provided by the spin-resolved two-body density matrix $\rho^{(\uparrow,\downarrow)}_{prqs}$, which for small R is peaked at $prqs = 0000$, signaling that the ground state is approximately a single Slater determinant. As R increases, $\rho^{(\uparrow,\downarrow)}_{0000} = \rho^{(\uparrow,\downarrow)}_{1111} \simeq 1/2$ and $\rho^{(\uparrow,\downarrow)}_{0101} =$

$\rho^{(\uparrow,\downarrow)}_{1010} \simeq -1/2$, signaling that the ground state is a linear combination of two closed-shell singlet wave functions.

C. QITE hardware experiments

In Fig. 8, we further investigate the ground-state potential-energy surface of NH_3 using the QITE method using the five-qubit *ibmq_vigo* and *ibmq_london* IBM quantum hardware. Details of QITE simulations, and especially
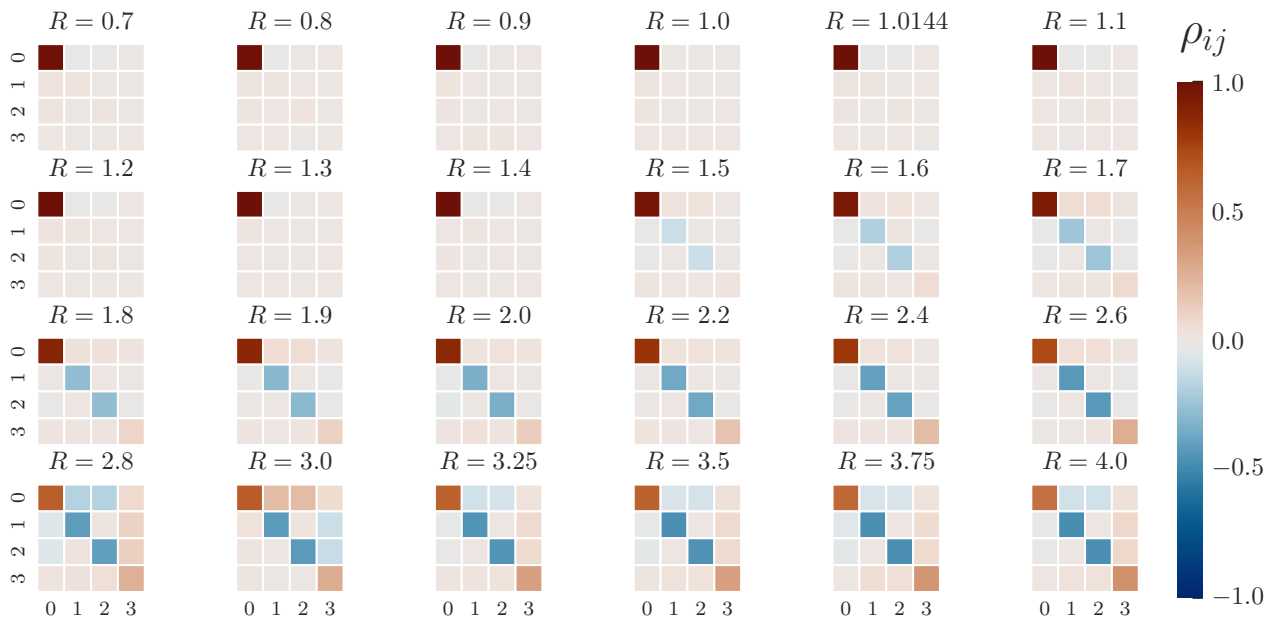

FIG. 7. Spin-resolved two-body density matrix $\rho^{(\uparrow,\downarrow)}$ for NH_3 in a HONO-LUNO space, from VQE with the SO(4) Ansatz as a function of N-H distance (left to right, top to bottom). Numbers 0–3 denote indices (0,0), (0,1), (1,0), and (1,1), respectively.
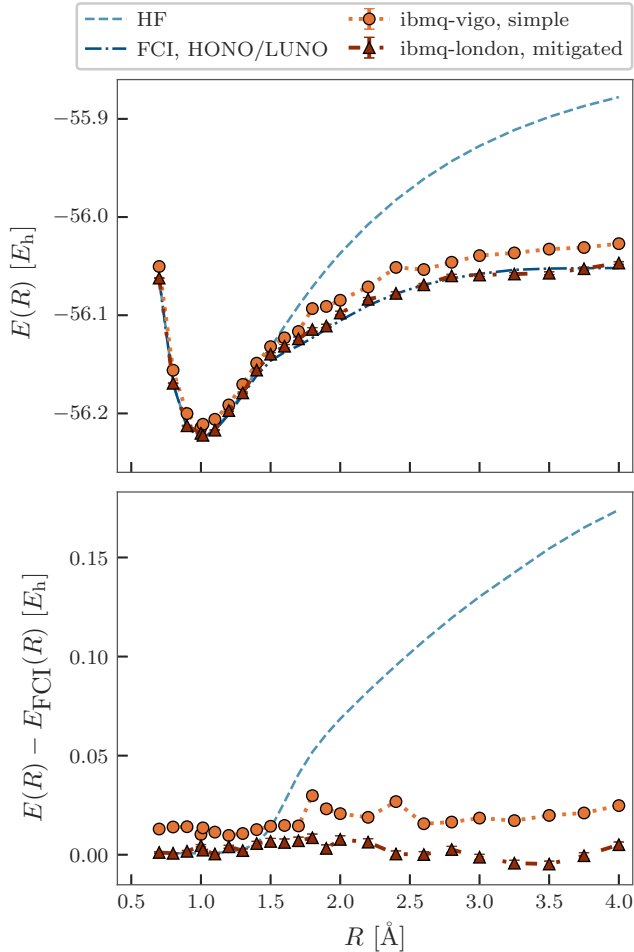
FIG. 8. Ground-state potential-energy surface of NH_3 along the $NH_3 \rightarrow NH_2 + H$ reaction path using quantum imaginary-time evolution without (orange circles) and with (red triangles) readout error mitigation on *ibmq_vigo* and *ibmq_london*, respectively.

simplifications made possible by the two-qubit nature of the problem, are given in Appendix D. In Fig. 8 and Table III we can appreciate the impact of readout error mitigation techniques [54,57,83,84] on the accuracy of QITE, in terms of deviations from FCI as well as equilibrium bond length and binding energy. Readout error mitigation has more pronounced effect on results in the regime $R \geqslant 1.75$ where the electronic wave function starts acquiring multireference character and deviating appreciably from the Hartree-Fock state. Therefore, it does not affect the equilibrium bond length

TABLE III. N-H dissociation energy, NH_3 equilibrium bond length, and deviation from FCI from RHF and QITE with and without error mitigation using a HONO-LUNO active space determined at the IAO-aug-cc-pVQZ level.

Method	ΔE (E_h)	R_{eq} (Å)	$\Delta_{RHF, QITE}$ (E_h)
RHF	N/A	0.995(1)	0.060
QITE, no mitigation	0.195(4)	1.002(9)	0.0169
QITE, mitigation	0.178(2)	0.993(7)	0.0036
FCI	0.180(2)	0.9961(7)	N/A

within statistical uncertainties, whereas it affects the binding energy of the system by $\sim 0.015 E_h$.

IV. DISCUSSION

In this paper, we explored the use of intrinsic atomic orbitals in lieu of minimal basis sets of Gaussian orbitals in quantum simulations of molecular systems. Bases of IAOs have the same size of minimal bases but offer more accurate estimates of energy differences and equilibrium geometries. IAOs arise from an exceptionally simple algebraic construction, require only mean-field calculations in larger basis sets to be defined, and draw a simple and effective connection between chemical concepts and numerical simulations. As such, they are a compelling alternative to minimal basis sets in quantum simulations, along with other recently proposed approaches [12,85], until the progress of hardware and classical simulators of quantum computers will allow to routinely study larger basis sets from systematic sequences.

The main limitation of IAOs is that electronic correlation is captured within a valence space. Therefore, perturbative or full inclusion of virtual orbitals is necessary to cover the dynamical correlations with methods, such as coupled cluster and multireference configuration interaction model, and very important to obtain quantitative agreement with experimental values especially for sensitive quantities, such as polarizabilities or thermochemical properties. The connection between IAOs and larger bases can be leveraged to perturbatively include virtual orbitals beyond the IAO in the simulation as we demonstrated here using a simplified implementation of VQSE for two-electron systems.

We expect that the combination of intrinsic atomic orbitals to partially overcome the limitations of minimal basis sets and of density operators to diagnose important properties of electronic wave functions will prove useful tools in the simulation of chemical species by quantum algorithms on contemporary quantum devices.

The code used to generate the data presented in this paper can be publicly accessed on GITHUB in Ref. [86].

APPENDIX A: COMPARISON OF IAO AGAINST OTHER BASES

In this Appendix, we compare IAO potential-energy curves along the NH_3 dissociation path, as binding energies, and equilibrium bond lengths against those from active spaces of low-energy Hartree-Fock, CASSCF orbitals, and
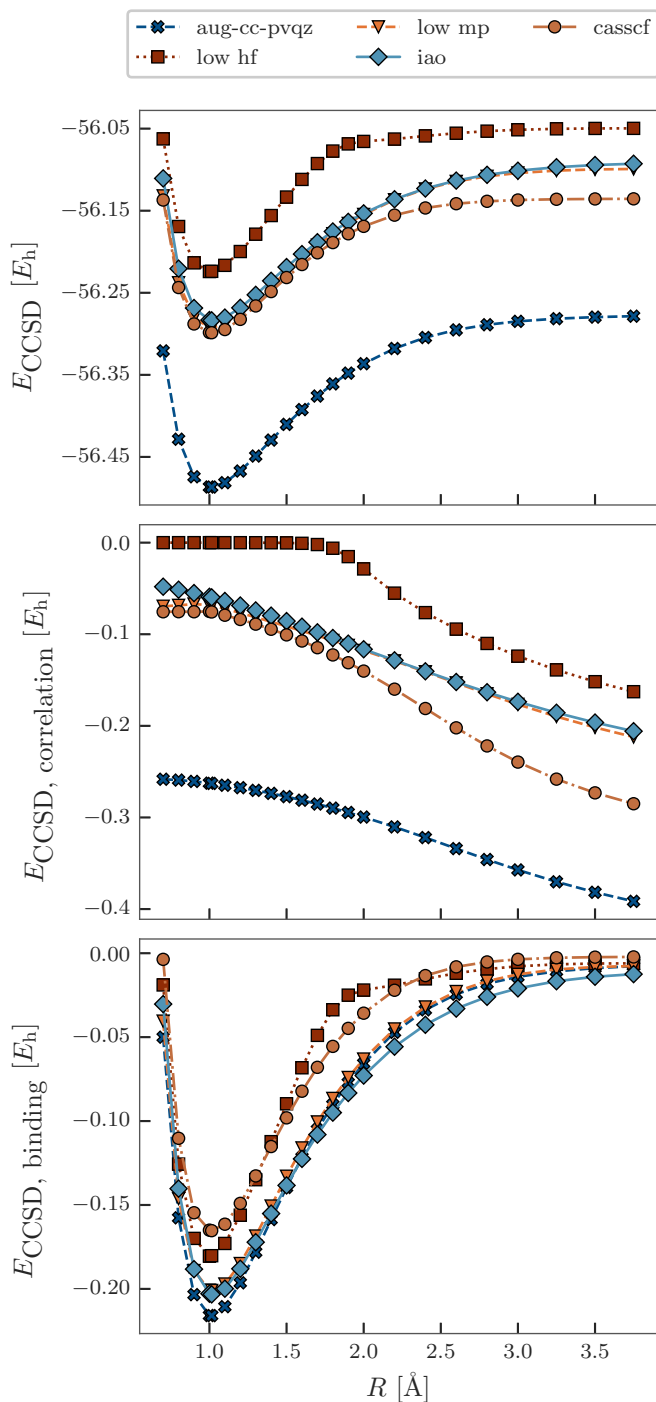
FIG. 9. CCSD total (top), correlation (middle), and binding (bottom) energies of NH_3 along the $NH_3 \rightarrow NH_2 + H$ dissociation path from CCSD/aug-cc-pVQZ (blue crosses), low-energy Hartree-Fock orbitals (red squares), low-energy CASSCF orbitals (dark orange circles), high-occupancy MP2 natural orbitals (orange triangles), and IAO/aug-cc-pVQZ (light blue diamonds).

high-occupancy MP2 natural orbitals. Results are given in Figs. 9 and 10, using CCSD at the aug-cc-pVQZ and cc-pVTZ levels. As seen, active spaces of low-energy Hartree-Fock give a lower-accuracy total, correlation, and binding energies than the other choices. We reason that the worse performance of low-energy Hartree-Fock orbitals is due to the
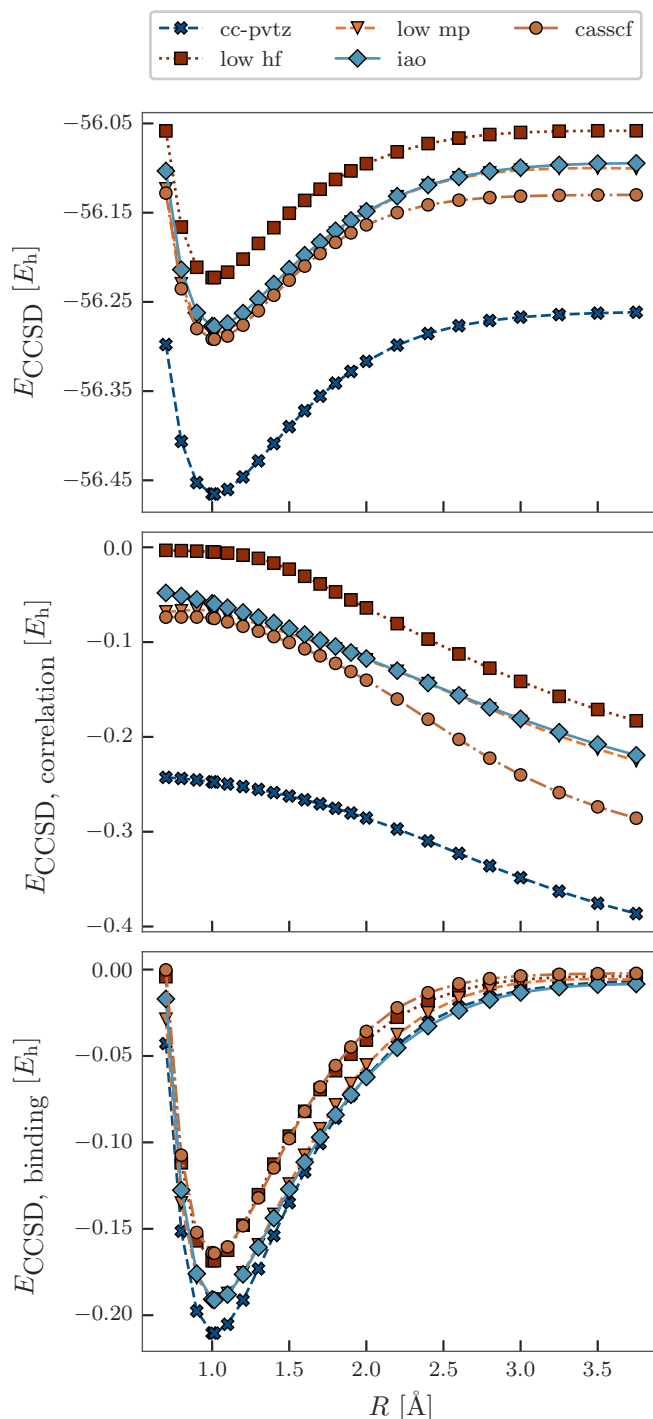

FIG. 10. Same as Fig. 9 but for cc-pVTZ.

inclusion of Rydberg, rather than antibonding, orbitals in the active space. IAO performs similarly to high-occupancy MP2 natural orbitals, and overall, they give binding energies in better agreement with CCSD/aug-cc-pVQZ than low-energy Hartree-Fock and CASSCF orbitals.

Compared against minimal bases, IAOs comprise higher-quality orbitals. Compared against larger basis sets, the main benefit of IAOs is the reduced number of orbitals and qubits. Numerical simulations with classical emulators employed $(N_\alpha, N_\beta) = (4, 4)$ and $(4,4)$ electrons, $N_{IAO} =$ six and seven

orbitals, and $N_{\text{qubit}} =$ eight and 11 qubits for water and ammonia, respectively.

APPENDIX B: QUANTUM EQUATION OF MOTION

In this Appendix we turn our attention to electronic excited states, that we investigate using the quantum equation-of-motion formalism. The quantum equation-of-motion (qEOM) [27,87,88] is a technique for approximating excited states of quantum systems by applying suitable excitation operators to their ground state,

$$|\Psi_I\rangle = \hat{O}_I^\dagger |\Psi_0\rangle. \tag{B1}$$

In general, excitation operators are arbitrarily complicated many-body operators. As in classical coupled-cluster calculations [89–91], accurate approximations for selected excited states are obtained assuming that excitation operators are low rank,

$$\hat{O}_I^\dagger = \sum_\mu X_{\mu I} \hat{E}_\mu - Y_{\mu I} \hat{E}_\mu^\dagger,$$

$$\hat{E}_\mu \in \left\{ \sum_\sigma \hat{c}_{a\sigma}^\dagger \hat{c}_{i\sigma}, \sum_{\sigma\tau} \hat{c}_{a\sigma}^\dagger \hat{c}_{b\tau}^\dagger \hat{c}_{j\tau} \hat{c}_{i\sigma} \right\}, \tag{B2}$$

where indices ij and ab label occupied and virtual orbitals in a mean-field reference state. The expansion coefficients are determined [27,92] solving a generalized eigenvalue equation of the form

$$\begin{bmatrix} M & Q \\ Q^* & M^* \end{bmatrix} \begin{bmatrix} X_I \\ Y_I \end{bmatrix} = \Delta E_I \begin{bmatrix} V & W \\ -W^* & -V^* \end{bmatrix} \begin{bmatrix} X_I \\ Y_I \end{bmatrix}, \tag{B3}$$

where matrix elements are defined as

$$\begin{aligned} V_{\mu\nu} &= \langle \Psi | [\hat{E}_\mu^\dagger, \hat{E}_\nu] | \Psi \rangle \\ M_{\mu\nu} &= \langle \Psi | [\hat{E}_\mu^\dagger, \hat{H}, \hat{E}_\nu] | \Psi \rangle \\ W_{\mu\nu} &= -\langle \Psi | [\hat{E}_\mu^\dagger, \hat{E}_\nu^\dagger] | \Psi \rangle \\ Q_{\mu\nu} &= -\langle \Psi | [\hat{E}_\mu^\dagger, \hat{H}, \hat{E}_\nu^\dagger] | \Psi \rangle, \end{aligned} \tag{B4}$$

and triple commutators have the form

$$[\hat{A}, \hat{B}, \hat{C}] = \frac{[[\hat{A}, \hat{B}], \hat{C}] + [\hat{A}, [\hat{B}, \hat{C}]]}{2}. \tag{B5}$$

1. qEOM hardware experiments

In Fig. 11 we show the qEOM energies of excited states in the HONO-LUNO subspace, using ibmq_rome with readout error mitigation. We mention that further mitigation of gate and readout error can be achieved by QST [87], but for the purpose of the present paper we elected to use the more standard readout error mitigation implemented in QISKIT and explained in Sec. II F.

The mean deviations between exact and computed excited-state energies is 0.019 784, 0.027 757, and 0.029 781 for the first, second, and third excited states, respectively. Of course, the use of a two-orbital active space determined the ability to detect only a subset of excited states, that around the equilibrium geometry are significantly biased (discontinuities at $R \simeq 1$ Å). In the long R limit, the ground and lowest
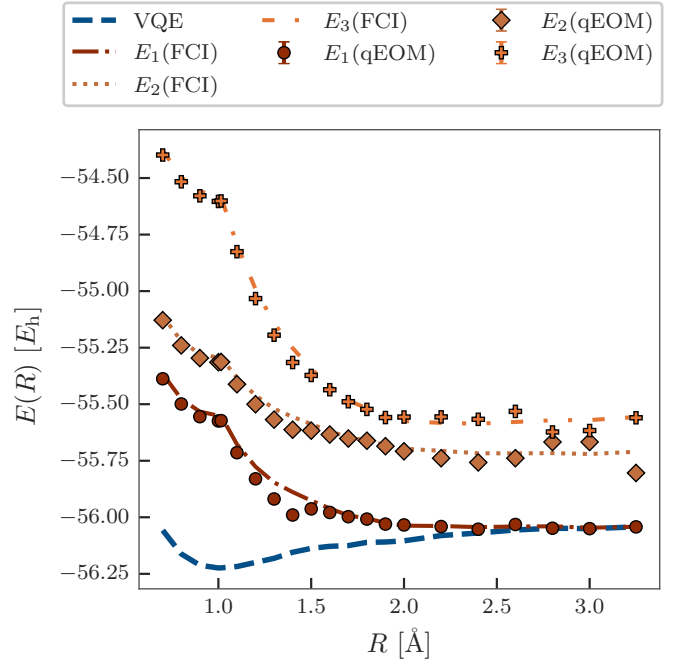

FIG. 11. Excited-state energies (brown-red, dark-orange, and orange for the first, second, and third excited states) of NH_3 along the $NH_3 \rightarrow NH_2 + H$ reaction path using FCI (lines) and qEOM (symbols), on the ibmq_rome IBM quantum hardware. $E_n(M)$ indicates the nth excited state obtained with method M. The blue dashed line indicates the energy calculated using the VQE on hardware.

excited states of triplet character become degenerate. Due to such degeneracy, the qEOM eigenvalue equation becomes ill conditioned as documented below, resulting in excited-state energies with lower accuracy than in the short R regime.

2. Details of qEOM simulations

Solving the qEOM equation $Hu_i = \epsilon_i Gu_i$ where we will call H and G the "Hamiltonian" and "metric" matrices, respectively, requires the metric matrix G to be numerically well conditioned, and, in particular, to have $|\det(G)| \gg 0$. In Fig. 12, we report the determinant $\det(G)$ of the metric matrix as a function of reaction coordinate R along the dissociation of ammonia. As seen, for $R \geqslant 2.5$, the determinant approaches zero, signaling the incipient degeneracy of singlet and triplet states.

APPENDIX C: DETAILS OF VQE SIMULATIONS

1. Optimization on quantum hardware

The variational parameters θ are concentrated, for both the SO(4) and the Ry Ansätze, in the angles of single-qubit rotations. Given a unitary $\hat{U}(\theta)$ where a parameter θ_μ appears in a single-qubit rotation only, it is known [73] that

$$\frac{\partial E}{\partial \theta_\mu}(\theta) = E(\theta_+) - E(\theta_-),$$

$$E(\theta_\pm) = E\left(\cdots \theta_\mu \pm \frac{\pi}{2} \cdots \right). \tag{C1}$$
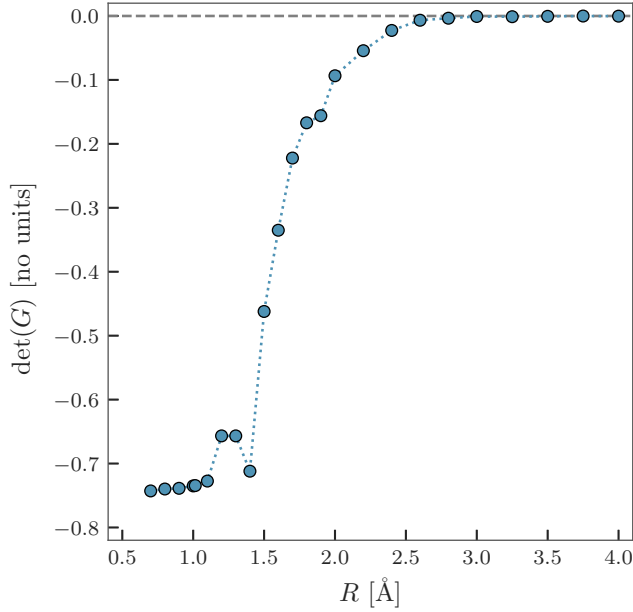
FIG. 12. Determinant of the qEOM metric matrix G as a function of reaction coordinate, measured on ibmq_rome (dotted, blue circles). The gray dashed line highlights $\det(G) = 0$.

Thus, the gradient of the VQE energy with the SO(4) Ansatz can be computed analytically with 12 n_{gates} energy measurements, where n_{gates} is the number of SO(4) gates in the circuit.

In Fig. 13 we demonstrate SO(4) parameter optimization by gradient descent at reaction coordinate $R = 3.0$ Å. In the gradient descent optimization scheme, parameters are initialized from a configuration $\theta^{(0)}$ in our case $\theta^{(0)} = 0$ and between iterations i and $i + 1$ are updated as

$$
\begin{aligned}
\vec{\theta}^{(i+1)} &= \vec{\theta}^{(i)} - \lambda^* \vec{g}^{(i)}, \\
\vec{g}^{(i)} &= \vec{\nabla} E(\vec{\theta}^{(i)}), \\
\lambda^* &= \operatorname{argmin}_\lambda E(\vec{\theta}^{(i)} - \lambda \vec{g}^{(i)}).
\end{aligned} \tag{C2}
$$

The gradient $\vec{g}^{(i)}$ is computed analytically as detailed above. The line search is performed manually at each iteration, and optimization continues until convergence of the energy within statistical uncertainties.

2. Fidelity between VQE and Hartree-Fock states

To gain further insight in the structure of the wave function, we used information from the measurement of density matrices to evaluate the fidelity,

$$
F[\rho_{\text{VQE}}, |\Psi_{\text{RHF}}\rangle\langle\Psi_{\text{RHF}}|] = \langle\Psi_{\text{RHF}}|\rho_{\text{VQE}}|\Psi_{\text{RHF}}\rangle, \tag{C3}
$$

between the VQE density operator and the projector onto the RHF state, shown in Fig. 14 as a function of reaction coordinate. Interestingly, both deviations from $S^2 = 0$ and decrease in purity are concomitant with the decrease in fidelity between VQE density operator and RHF, starting at $R \geqslant 1.5$ Å, and
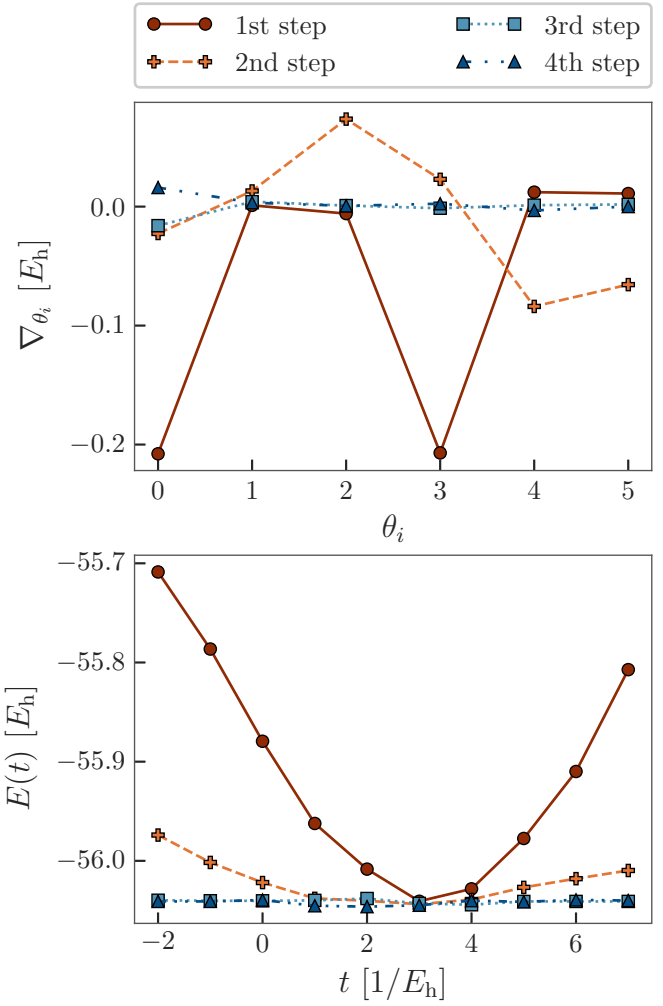

FIG. 13. Analytical gradient evaluation (top) and line search (bottom) in the gradient-descent optimization of VQE parameters with the SO(4) Ansatz.

signaling acquisition of multireference character by the VQE density operator.

APPENDIX D: DETAILS OF QITE SIMULATIONS

In the QITE simulations performed here, we use a time-step $\Delta\tau = 0.5E_{\text{h}}$ and a total projection time $\beta = 7.0E_{\text{h}}$. Since the Hamiltonian $\hat{H}$ is a two-qubit operator, we perform imaginary-time evolution under the operator $\hat{H}$ without Trotter-Suzuki or similar approximations.

To keep the circuit depth and the number of CNOT gates in the QITE circuit constant as β increases, we rely on a KAK decomposition [93]: the QITE unitary for n time-steps U_n is computed on the classical computer and reduced to a quantum circuit comprising two CNOT gates [93].

Such a technique, used, for example, in the context of spin simulations [94,95], is specifically designed for two-qubit systems. Research to generalize these approximations to more general situations is underway.
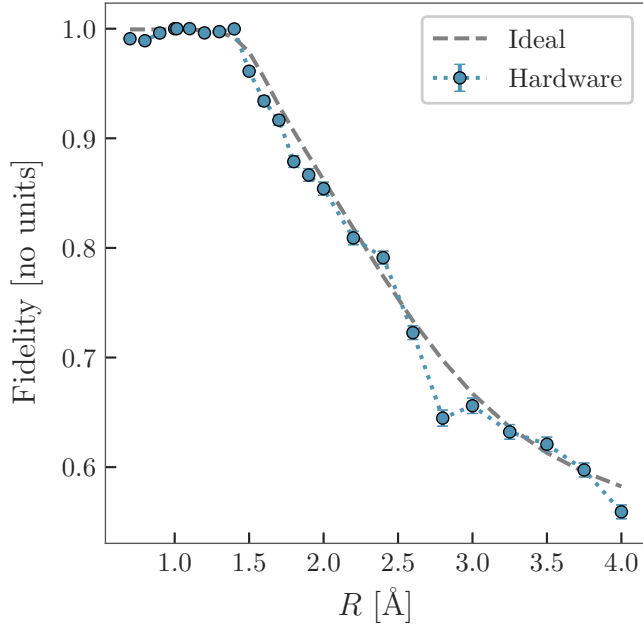
FIG. 14. Fidelity between the VQE density operator and the projector onto the RHF state as a function of reaction coordinate. The gray dotted line indicates the ideal result of a state vector simulation. The blue circles are the results of the experiment on *ibmq_rome*.

APPENDIX E: VARIATIONAL QUANTUM SUBSPACE EXPANSION

In this Appendix, we review briefly VQSE technique, proposed by Takeshita *et al.* [12], and calculate the explicit expression of matrix elements for our problem. We show that all the matrices can be evaluated using data from a quantum hardware.

As indicated in the main text, the starting point of VQSE is a reference function Ψ_0 constructed in a set of active orbitals from a large basis. Here, active-space orbitals are linear combinations of IAOs, denoted with lowercase letters $p \in A$. Uppercase letters $P \in B_1$ denote orthonormal orbitals in the basis used to construct IAOs.

Next, VQSE introduces a set of expansion operators. Here, we choose

$$|\Psi\rangle = [\alpha + \beta_{Pr}\hat{c}^\dagger_{P\sigma}\hat{c}_{r\sigma} + \gamma_{TuVw}\hat{c}^\dagger_{T\sigma}\hat{c}^\dagger_{V\tau}\hat{c}_{w\tau}\hat{c}_{u\sigma}]|\Psi_0\rangle$$
$$= [\alpha + \beta_{Pr}E_{Pr} + \gamma_{TuVw}E_{TuVw}]|\Psi_0\rangle. \quad (E1)$$

Electrons are excited from active to generic orbitals, excitation operators are summed over spin polarizations σ, τ, and Einstein's summation convention is used. Note that the reference wave function has no components outside the active space A, and, therefore, contraction over orbitals outside A can be computed analytically using Wick's theorem.

The amplitudes $v = (\alpha \; \beta \; \gamma)^T$ are real valued and determined by solving a generalized eigenvalue equation $Hv = ESv$.

The matrices H and S are defined by the bilinear forms

$$\langle\Psi|\Psi\rangle = (\alpha, \beta_{Qs}, \gamma_{XyZa})$$
$$\times \begin{pmatrix} 1 & \langle\hat{E}_{Pr}\rangle & \langle\hat{E}_{TuVw}\rangle \\ \langle\hat{E}_{sQ}\rangle & \langle\hat{E}_{sQ}E_{Pr}\rangle & \langle\hat{E}_{sQ}\hat{E}_{TuVw}\rangle \\ \langle\hat{E}_{yXaZ}\rangle & \langle\hat{E}_{yXaZ}E_{Pr}\rangle & \langle\hat{E}_{yXaZ}\hat{E}_{TuVw}\rangle \end{pmatrix}$$
$$\times \begin{pmatrix} \alpha \\ \beta_{Pr} \\ \gamma_{TuVw} \end{pmatrix},$$

$$\langle\Psi|\hat{H}|\Psi\rangle = (\alpha, \beta_{Qs}, \gamma_{XyZa})$$
$$\times \begin{pmatrix} \langle\hat{H}\rangle & \langle\hat{H}\hat{E}_{Pr}\rangle & \langle\hat{H}\hat{E}_{TuVw}\rangle \\ \langle\hat{E}_{sQ}\hat{H}\rangle & \langle\hat{E}_{sQ}\hat{H}\hat{E}_{Pr}\rangle & \langle\hat{E}_{sQ}\hat{H}\hat{E}_{TuVw}\rangle \\ \langle\hat{E}_{yXaZ}\hat{H}\rangle & \langle\hat{E}_{yXaZ}\hat{H}\hat{E}_{pr}\rangle & \langle\hat{E}_{yXaZ}\hat{H}\hat{E}_{TuVw}\rangle \end{pmatrix}$$
$$\times \begin{pmatrix} \alpha \\ \beta_{Pr} \\ \gamma_{TuVw} \end{pmatrix}. \quad (E2)$$

Here, $\hat{H} = T_{EFGH}\hat{c}^\dagger_{E\sigma}\hat{c}^\dagger_{G\tau}\hat{c}_{H\tau}\hat{c}_{F\sigma}$ denotes the Hamiltonian, written compactly as a two-body operator, and angular brackets denote expectation values over the reference state.

In the present paper, we focused on two-electron problems where the bilinear forms in Eq. (E2) are defined by the full-basis one- and two-body density matrices, which, in turn, can be trivially computed given their active-space counterparts [12].

A lengthy but straightforward calculation, based on Wick's theorem, shows that the bilinear forms in Eq. (E2) are given by

$$\langle\hat{E}_{Pr}\rangle = \rho_{Pr},$$
$$\langle\hat{E}_{TuVw}\rangle = \rho_{TuVw},$$
$$\langle\hat{E}_{sQ}\rangle = \rho_{sQ},$$
$$\langle\hat{E}_{sQ}\hat{E}_{Pr}\rangle = \delta_{PQ}\rho_{sr} + \rho_{PrsQ},$$
$$\langle\hat{E}_{sQ}\hat{E}_{TuVw}\rangle = \delta_{QT}\rho_{suVw} - \delta_{QV}\rho_{suTw},$$
$$\langle\hat{E}_{yXaZ}\rangle = \rho_{aZyX},$$
$$\langle\hat{E}_{yXaZ}\hat{E}_{Pr}\rangle = \delta_{XP}D_{aZyr} - \delta_{ZP}D_{yraX},$$
$$\langle\hat{E}_{yXaZ}\hat{E}_{TuVw}\rangle = [\delta_{XT}\delta_{VZ} - \delta_{ZT}\delta_{XV}]D_{awyu}, \quad (E3)$$
$$\langle\hat{H}\hat{E}_{Pr}\rangle = T_{EPGH}\rho_{ErGH} + T_{EFGP}\rho_{EFGr},$$
$$\langle\hat{H}\hat{E}_{TuVw}\rangle = T_{EVGT}\rho_{EwGu} + T_{ETGV}\rho_{EuGw},$$
$$\langle\hat{E}_{sQ}\hat{H}\rangle = T_{QFGH}\rho_{GHsF} + T_{EFGH}\rho_{EFsH},$$
$$\langle\hat{E}_{sQ}\hat{H}\hat{E}_{Pr}\rangle = T_{QFGP}\rho_{GrsF} + T_{QPGH}\rho_{GHsr}$$
$$+ T_{EFQP}\rho_{QFsr} + T_{EPQH}\rho_{ErsH},$$
$$\langle\hat{E}_{sQ}\hat{H}\hat{E}_{TuVw}\rangle = T_{QTGV}\rho_{Gwsu} + T_{EVQT}\rho_{Ewsu}$$
$$+ T_{QVGT}\rho_{Gusw} + T_{ETQV}\rho_{Eusw},$$
$$\langle\hat{E}_{yXaZ}\hat{H}\rangle = T_{XFZH}\rho_{aHyF} + T_{ZFXH}\rho_{aFyH},$$
$$\langle\hat{E}_{yXaZ}\hat{H}\hat{E}_{Pr}\rangle = T_{XFZP}\rho_{aryF} + T_{ZFXP}\rho_{aFyr}$$
$$+ T_{ZPXH}\rho_{aryH} + T_{XPZH}\rho_{aHyr},$$
$$\langle\hat{E}_{yXaZ}\hat{H}\hat{E}_{TuVw}\rangle = [T_{ZVXT} + T_{XTZV}]\rho_{awyu}$$
$$+ [T_{ZTXV} + T_{XVZT}]\rho_{auyw}.$$

Importantly, the simplifications in Eq. (E3) hold for two-electron active spaces. Otherwise, three- and four-body active-space density matrices are required by VQSE, leading to an $O(N_o^8)$ computational cost in the number N_o of active orbitals. Active-space density matrices were computed with the techniques seen in the main text and embedded into their full-basis counterparts.

[1] R. P. Feynman, Int. J. Theor. Phys. **21**, 467 (1982).

[2] S. Lloyd, Science **273**, 1073 (1996).

[3] D. S. Abrams and S. Lloyd, Phys. Rev. Lett. **79**, 2586 (1997).

[4] I. M. Georgescu, S. Ashhab, and F. Nori, Rev. Mod. Phys. **86**, 153 (2014).

[5] Y. Cao, J. Romero, J. P. Olson, M. Degroote, P. D. Johnson, M. Kieferová, I. D. Kivlichan, T. Menke, B. Peropadre, N. P. Sawaya *et al.*, Chem. Rev. **119**, 10856 (2019).

[6] S. McArdle, S. Endo, A. Aspuru-Guzik, S. C. Benjamin, and X. Yuan, Rev. Mod. Phys. **92**, 015003 (2020).

[7] B. Bauer, S. Bravyi, M. Motta, and G. K.-L. Chan, Chem. Rev. **120**, 12685 (2020).

[8] A. Kandala, A. Mezzacapo, K. Temme, M. Takita, M. Brink, J. M. Chow, and J. M. Gambetta, Nature (London) **549**, 242 (2017).

[9] P. J. J. O'Malley, R. Babbush, I. D. Kivlichan, J. Romero, J. R. McClean, R. Barends, J. Kelly, P. Roushan, A. Tranter, N. Ding, B. Campbell, Y. Chen, Z. Chen, B. Chiaro, A. Dunsworth, A. G. Fowler, E. Jeffrey, E. Lucero, A. Megrant, J. Y. Mutus, M. Neeley, C. Neill, C. Quintana, D. Sank, A. Vainsencher, J. Wenner, T. C. White, P. V. Coveney, P. J. Love, H. Neven, A. Aspuru-Guzik, and J. M. Martinis, Phys. Rev. X **6**, 031007 (2016).

[10] J. E. Rice, T. P. Gujarati, M. Motta, T. Y. Takeshita, E. Lee, J. A. Latone, and J. M. Garcia, J. Chem. Phys. **154**, 134115 (2021).

[11] Q. Gao, H. Nakamura, T. P. Gujarati, G. O. Jones, J. E. Rice, S. P. Wood, M. Pistoia, J. M. Garcia, and N. Yamamoto, J. Phys. Chem. A **125**, 1827 (2021).

[12] T. Takeshita, N. C. Rubin, Z. Jiang, E. Lee, R. Babbush, and J. R. McClean, Phys. Rev. X **10**, 011004 (2020).

[13] M. Motta, T. P. Gujarati, J. E. Rice, A. Kumar, C. Masteran, J. A. Latone, E. Lee, E. F. Valeev, and T. Y. Takeshita, Phys. Chem. Chem. Phys. **22**, 24270 (2020).

[14] G. Knizia, J. Chem. Theory Comput. **9**, 4834 (2013).

[15] B. Senjean, S. Sen, M. Repisky, G. Knizia, and L. Visscher, J. Chem. Theory Comput. **17**, 1337 (2021).

[16] M. Schwilk, Q. Ma, C. Köppl, and H.-J. Werner, J. Chem. Theory Comput. **13**, 3650 (2017).

[17] T. A. Manz and N. G. Limas, RSC Adv. **6**, 47771 (2016).

[18] A. C. West, M. W. Schmidt, M. S. Gordon, and K. Ruedenberg, J. Chem. Phys. **139**, 234107 (2013).

[19] E. R. Sayfutyarova, Q. Sun, G. K.-L. Chan, and G. Knizia, J. Chem. Theory Comput. **13**, 4063 (2017).

[20] W. B. Schneider, G. Bistoni, M. Sparta, M. Saitow, C. Riplinger, A. A. Auer, and F. Neese, J. Chem. Theory Comput. **12**, 4778 (2016).

[21] T. H. Dunning, Jr., J. Chem. Phys. **90**, 1007 (1989).

[22] J. Foster and S. Boys, Rev. Mod. Phys. **32**, 300 (1960).

[23] M. Born and R. Oppenheimer, Ann. Phys. (Berlin) **389**, 457 (1927).

[24] A. Peruzzo, J. McClean, P. Shadbolt, M.-H. Yung, X.-Q. Zhou, P. J. Love, A. Aspuru-Guzik, and J. L. O'Brien, Nat. Commun. **5**, 4213 (2014).

[25] J. R. McClean, J. Romero, R. Babbush, and A. Aspuru-Guzik, New J. Phys. **18**, 023023 (2016).

[26] M. Motta, C. Sun, A. T. Tan, M. J. O'Rourke, E. Ye, A. J. Minnich, F. G. Brandão, and G. K.-L. Chan, Nat. Phys. **16**, 205 (2020).

[27] P. J. Ollitrault, A. Kandala, C.-F. Chen, P. K. Barkoutsos, A. Mezzacapo, M. Pistoia, S. Sheldon, S. Woerner, J. M. Gambetta, and I. Tavernelli, Phys. Rev. Research **2**, 043140 (2020).

[28] W. Kutzelnigg, J. Chem. Phys. **77**, 3081 (1982).

[29] W. Kutzelnigg and S. Koch, J. Chem. Phys. **79**, 4315 (1983).

[30] W. Kutzelnigg, J. Chem. Phys. **82**, 4166 (1985).

[31] P. K. Barkoutsos, J. F. Gonthier, I. Sokolov, N. Moll, G. Salis, A. Fuhrer, M. Ganzhorn, D. J. Egger, M. Troyer, A. Mezzacapo, S. Filipp, and I. Tavernelli, Phys. Rev. A **98**, 022322 (2018).

[32] F. Vatan and C. Williams, Phys. Rev. A **69**, 032315 (2004).

[33] K. Yeter-Aydeniz, R. C. Pooser, and G. Siopsis, npj Quantum Inf. **6**, 63 (2020).

[34] K. Yeter-Aydeniz, G. Siopsis, and R. C. Pooser, arXiv:2008.08763

[35] H. Nishi, T. Kosugi, and Y.-I. Matsushita, npj Quantum Inf. **7**, 85 (2021).

[36] N. Gomes, F. Zhang, N. F. Berthusen, C.-Z. Wang, K.-M. Ho, P. P. Orth, and Y. Yao, J. Chem. Theory Comput. **16**, 6256 (2020).

[37] P.-O. Löwdin, Phys. Rev. **97**, 1474 (1955).

[38] P.-O. Löwdin, Phys. Rev. **97**, 1490 (1955).

[39] P.-O. Löwdin, Phys. Rev. **97**, 1509 (1955).

[40] H.-J. Werner and P. J. Knowles, J. Chem. Phys. **82**, 5053 (1985).

[41] M. Head-Gordon and J. A. Pople, J. Phys. Chem. **92**, 3063 (1988).

[42] C. D. Sherrill, A. I. Krylov, E. F. Byrd, and M. Head-Gordon, J. Chem. Phys. **109**, 4171 (1998).

[43] P. Jordan and E. P. Wigner, in *The Collected Works of Eugene Paul Wigner* (Springer, Berlin, 1993), pp. 109–129.

[44] S. B. Bravyi and A. Y. Kitaev, Ann. Phys. (NY) **298**, 210 (2002).

[45] J. T. Seeley, M. J. Richard, and P. J. Love, J. Chem. Phys. **137**, 224109 (2012).

[46] Q. Sun, T. C. Berkelbach, N. S. Blunt, G. H. Booth, S. Guo, Z. Li, J. Liu, J. D. McClain, E. R. Sayfutyarova, S. Sharma *et al.*, WIREs Comput. Mol. Sci. **8**, e1340 (2018).

[47] Q. Sun *et al.*, J. Chem. Phys. **153**, 024109 (2020).

[48] C. Møller and M. S. Plesset, Phys. Rev. **46**, 618 (1934).

[49] G. Aleksandrowicz, T. Alexander, P. Barkoutsos, L. Bello, Y. Ben-Haim, D. Bucher, F. Cabrera-Hernández, J. Carballo-Franquis, A. Chen, C. Chen *et al.*, Zenodo **16** (2019), https://doi.org/10.5281/zenodo.2573505.

[50] S. Bravyi, J. M. Gambetta, A. Mezzacapo, and K. Temme, arXiv:1701.08213.

[51] K. Setia, R. Chen, J. E. Rice, A. Mezzacapo, M. Pistoia, and J. D. Whitfield, J. Chem. Theory Comput. **16**, 6091 (2020).

[52] C. Zhu, R. H. Byrd, P. Lu, and J. Nocedal, ACM Trans. Math. Softw. **23**, 550 (1997).

[53] J. L. Morales and J. Nocedal, ACM Trans. Math. Softw. **38**, 1 (2011).

[54] K. Temme, S. Bravyi, and J. M. Gambetta, Phys. Rev. Lett. **119**, 180509 (2017).

[55] P. D. Nation, H. Kang, N. Sundaresan, and J. M. Gambetta, PRX Quantum **2**, 040326 (2021).

[56] Y. Li and S. C. Benjamin, Phys. Rev. X **7**, 021050 (2017).

[57] A. Kandala, K. Temme, A. D. Córcoles, A. Mezzacapo, J. M. Chow, and J. M. Gambetta, Nature (London) **567**, 491 (2019).

[58] A. Carbone, D. E. Galli, M. Motta, and B. Jones, Symmetry **14**, 624 (2022).

[59] K. Yeter-Aydeniz, G. Siopsis, and R. C. Pooser, New J. Phys. **23**, 043033 (2021).

[60] Y. Shao, L. F. Molnar, Y. Jung, J. Kussmann, C. Ochsenfeld, S. T. Brown, A. T. Gilbert, L. V. Slipchenko, S. V. Levchenko, D. P. O'Neill *et al.*, Phys. Chem. Chem. Phys. **8**, 3172 (2006).

[61] W. Baader, C. Stevani, E. Bastos, and Z. Rappoport, *The Chemistry of Peroxides* (Wiley, Hoboken, NJ, 2006).

[62] P. Å. Malmqvist, K. Pierloot, A. R. M. Shahi, C. J. Cramer, and L. Gagliardi, J. Chem. Phys. **128**, 204109 (2008).

[63] C. J. Stein and M. Reiher, J. Chem. Theory Comput. **12**, 1760 (2016).

[64] B. O. Roos, P. Linse, P. E. Siegbahn, and M. R. Blomberg, Chem. Phys. **66**, 197 (1982).

[65] K. Andersson, P. A. Malmqvist, B. O. Roos, A. J. Sadlej, and K. Wolinski, J. Phys. Chem. **94**, 5483 (1990).

[66] K. Andersson, P.-Å. Malmqvist, and B. O. Roos, J. Chem. Phys. **96**, 1218 (1992).

[67] C. Angeli, R. Cimiraglia, S. Evangelisti, T. Leininger, and J.-P. Malrieu, J. Chem. Phys. **114**, 10252 (2001).

[68] C. Angeli, R. Cimiraglia, and J.-P. Malrieu, Chem. Phys. Lett. **350**, 297 (2001).

[69] C. Angeli, R. Cimiraglia, and J.-P. Malrieu, J. Chem. Phys. **117**, 9138 (2002).

[70] J. Čížek, J. Chem. Phys. **45**, 4256 (1966).

[71] A. Eddins, M. Motta, T. P. Gujarati, S. Bravyi, A. Mezzacapo, C. Hadfield, and S. Sheldon, PRX Quantum **3**, 010309 (2022).

[72] A. Zulehner and R. Wille, in *24th Asia and South Pacific Design Automation Conference ASP-DAC 2019* (Springer, Berlin, 2019), pp. 185–190.

[73] R. M. Parrish, E. G. Hohenstein, P. L. McMahon, and T. J. Martinez, arXiv:1906.08728.

[74] J. J. Longdell and M. J. Sellars, Phys. Rev. A **69**, 032307 (2004).

[75] M. Steffen, M. Ansmann, R. C. Bialczak, N. Katz, E. Lucero, R. McDermott, M. Neeley, E. M. Weig, A. N. Cleland, and J. M. Martinis, Science **313**, 1423 (2006).

[76] F. A. Bonk, R. S. Sarthour, E. R. deAzevedo, J. D. Bulnes, G. L. Mantovani, J. C. C. Freitas, T. J. Bonagamba, A. P. Guimarães, and I. S. Oliveira, Phys. Rev. A **69**, 042322 (2004).

[77] X. Ma, T. Jackson, H. Zhou, J. Chen, D. Lu, M. D. Mazurek, K. A. G. Fisher, X. Peng, D. Kribs, K. J. Resch, Z. Ji, B. Zeng, and R. Laflamme, Phys. Rev. A **93**, 032140 (2016).

[78] D. Leibfried, D. M. Meekhof, B. E. King, C. Monroe, W. M. Itano, and D. J. Wineland, Phys. Rev. Lett. **77**, 4281 (1996).

[79] J. F. Poyatos, J. I. Cirac, and P. Zoller, Phys. Rev. Lett. **78**, 390 (1997).

[80] R. Blume-Kohout, J. K. Gamble, E. Nielsen, J. Mizrahi, J. D. Sterk, and P. Maunz, arXiv:1310.4492.

[81] S. T. Merkel, J. M. Gambetta, J. A. Smolin, S. Poletto, A. D. Córcoles, B. R. Johnson, C. A. Ryan, and M. Steffen, Phys. Rev. A **87**, 062119 (2013).

[82] D. Greenbaum, arXiv:1509.02921.

[83] S. McArdle, X. Yuan, and S. Benjamin, Phys. Rev. Lett. **122**, 180501 (2019).

[84] S. Bravyi, S. Sheldon, A. Kandala, D. C. Mckay, and J. M. Gambetta, Phys. Rev. A **103**, 042605 (2021).

[85] J. S. Kottmann, P. Schleich, T. Tamayo-Mendoza, and A. Aspuru-Guzik, J. Phys. Chem. Lett. **12**, 663 (2021).

[86] S. Barison *et al.*, GITHUB repository (2020), https://github.com/StefanoBarison/quantum_simulation_with_IAO.

[87] Q. Gao, G. O. Jones, M. Motta, M. Sugawara, H. C. Watanabe, T. Kobayashi, E. Watanabe, Y.-y. Ohnishi, H. Nakamura, and N. Yamamoto, npj Comput. Mater. **7**, 70 (2021).

[88] P. J. Ollitrault, A. Baiardi, M. Reiher, and I. Tavernelli, Chem. Sci. **11**, 6842 (2020).

[89] H. J. Monkhorst, Int. J. Quantum Chem. **12**, 421 (1977).

[90] J. F. Stanton and R. J. Bartlett, J. Chem. Phys. **98**, 7029 (1993).

[91] A. I. Krylov, Acc. Chem. Res. **39**, 83 (2006).

[92] D. Rowe, Rev. Mod. Phys. **40**, 153 (1968).

[93] B. Kraus and J. I. Cirac, Phys. Rev. A **63**, 062309 (2001).

[94] A. Francis, J. K. Freericks, and A. F. Kemper, Phys. Rev. B **101**, 014411 (2020).

[95] S.-N. Sun, M. Motta, R. N. Tazhigulov, A. T. Tan, G. K.-L. Chan, and A. J. Minnich, PRX Quantum **2**, 010317 (2021).